Synthesis, characterization, photocatalytic evaluation, and toxicity studies of TiO$_2$–Fe^{3+} nanocatalyst

Iliana Medina-Ramírez · Jingbo Louise Liu · Araceli Hernández-Ramírez · Cristina Romo-Bernal · Gladis Pedroza-Herrera · Juan Jáuregui-Rincón · Miguel A. Gracia-Pinilla

Abstract Based on our previous work on the green preparation of Ag–TiO$_2$ photocatalyst with bactericidal activity under visible light, we extended our studies to the synthesis of TiO$_2$–Fe^{3+} materials with enhanced photocatalytic activity for the degradation of recalcitrant organic pollutants in water. TiO$_2$–Fe^{3+} nanopowders were synthesized using a robust, environmentally friendly procedure. Established amounts of Fe(NO$_3$)$_3$·9H$_2$O and titanium tetraisopropoxide (TTIP) were mixed using glacial acetic acid as solvent. Hydrolysis of TTIP–Fe^{3+} was accomplished using a 30 % (W/V) Arabic gum aqueous solution. TiO$_2$–Fe^{3+} nanopowders were obtained by thermal treatment at 400 °C. In order to elucidate the structure of these photocatalysts, microscopic and spectroscopic characterization techniques were applied. The high resolution transmission electron microscopy (HRTEM) analysis indicated the presence of uniformly distributed particles with average particle size of about 9 nm. According to the HRTEM lattice fringes, ring pattern, and selected area electron diffraction pattern, the crystalline part of the samples consists of *anatase* (PDF 01-086-1157 with the lattice constant of 3.7852, 9.5139 Å and 90°) as dominant phase. X-ray photoelectron spectroscopy (XPS) was applied to determine the oxidation state of iron. The XPS provides evidence for Fe^{3+} surface species in the TiO$_2$–Fe^{3+} composite. Complete degradation of aqueous solutions (20 ppm) of methylene blue and/or methyl orange was accomplished after 4 h of treatment using 150 mg of

I. Medina-Ramírez (✉) · C. Romo-Bernal · G. Pedroza-Herrera
Departamento de Química, Universidad Autónoma de Aguascalientes, Av. Universidad 940, Ciudad Universitaria, 20131 Aguascalientes, Ags., Mexico
e-mail: iemedina@correo.uaa.mx

J. L. Liu
Chemistry Department, Texas A&M University-Kingsville, MSC 161, 700 University Blvd, Kingsville, TX 78363, USA
e-mail: kfjll00@tamuk.edu

J. L. Liu
Chemical Biology Research Group (CBRG), Chemistry Department, Texas A&M University-Kingsville, MSC 161, 700 University Blvd, Kingsville, TX 78363, USA

A. Hernández-Ramírez
Laboratorio de Foto-catálisis y Electroquímica Ambiental, Facultad de Ciencias Químicas, Universidad Autónoma de Nuevo León, Av. Universidad, Cd. Universitaria, San Nicolás de los Garza, N.L., Mexico
e-mail: aracely.hernandezrm@uanl.edu.mx

J. Jáuregui-Rincón
Departamento de Ingeniería Bioquímica, Universidad Autónoma de Aguascalientes, Av. Universidad 940, Ciudad Universitaria, 20131 Aguascalientes, Ags., Mexico
e-mail: jjaureg@correo.uaa.mx

M. A. Gracia-Pinilla
Facultad de Ciencias Físico-Matemáticas, Universidad Autónoma de Nuevo León, Av. Universidad, Cd. Universitaria, San Nicolás de los Garza, N.L., Mexico
e-mail: miguelchem@gmail.com

M. A. Gracia-Pinilla
Centro de Investigación e Innovación en Desarrollo en Ingeniería y Tecnología, Universidad Autónoma de Nuevo León, Avenida Alianza 101 Sur PIIT, Apodaca, N.L. 66600, Mexico

TiO$_2$–Fe^{3+}/150 mL of dye solution. The in vitro toxicity of the materials was tested. The materials showed no toxicity against human red blood cells.

Introduction

The increasing volume and complexity of wastewater containing non-biodegradable pollutants discharged into the environment demand the development of new, powerful, clean, and safe decontamination techniques. Visible light active photocatalysis (doped TiO$_2$) is of special interest since sunlight can be used as energy source for the process, reducing wastewater treatment costs, and rendering sustainability by saving electricity [1]. Heterogeneous photocatalysis is based on the use of a wide-band-gap semiconductor, where photo excitement of a valence band electron leads to several reactions and production of hydroxyl radicals (·OH), which are able to oxidize and mineralize almost any organic molecule, yielding carbon dioxide (CO$_2$) and inorganic ions [2].

Titanium dioxide (TiO$_2$) is the most widely used catalyst due to its outstanding electronic properties and chemical stability. Industrial applications of this material have been delayed due to its large band gap that confers absorption properties in the UV region. Recently, numerous reports regarding doping of titania materials with transition metals have appeared, aiming at fabricating visible light active materials [3]. Iron doping has been studied widely since modification of the spectral response of TiO$_2$ into the visible range through the substitution of Fe^{3+} for Ti^{4+} has been observed [4]; nevertheless, the results as to whether iron doping (and the doping level) enhances the photoactivity of materials are contradictory; thus, there is a need to elucidate the role of iron doping in this material. When Fe^{3+} reduces to Fe^{2+} due to the trapping of electrons, its stable electronic configuration (d^5) is destroyed and stability decreases; in this way, the trapped electrons can easily be transferred to the oxygen adsorbed on the TiO$_2$ surface. This may promote charge transfer and the efficient separation of the electrons and holes [5]. Avoiding the electron/hole recombination can significantly improve the photo-reactivity of TiO$_2$–Fe^{3+} by acting both as hole and electron traps. However, there exists an optimum dopant concentration for the best photocatalytic performance of Fe^{3+}-doped TiO$_2$. It has been encountered that doping levels up to ca. 1 wt% allow the effective introduction of Fe^{3+} cation into the anatase structure along with associated modifications of the surface acid–base properties of the material [6].

On the other hand, higher doping levels result detrimental to the photoactivity of TiO$_2$–Fe^{3+} materials due to

segregation of amorphous iron oxides to the surface of the photocatalyst. In particular, Litter and Navio [7] have reported the lack of catalytic activity in 10 wt% Fe-doped anatase under visible light despite optical absorption in that region. In highly doped materials, the suppression of photoactivity can be ascribed to a high recombination rate of generated electron–hole pairs, as a result of the influence of dopant ions in TiO$_2$ matrix. There are some recent reports on the preparation of Fe(III)–Fe$_x$Ti$_{1-x}$O$_2$ nanocomposites that exhibit high photocatalytic reaction rates under visible light due to the presence of iron ions both at the surface of the catalyst and in substitutional (for Ti^{+4}) sites of TiO$_2$ lattice [8]. Also, Fe^{+3}-grafted N-doped TiO$_2$ nanoporous spheres were synthesized and fully characterized. The nanoporous TiO$_2$ spheres were fabricated by a two-step process (hydrolysis followed by hydrothermal reaction), and later doping of nitrogen and grafting of Fe^{+3} were accomplished by treating the sample with NH$_3$ in a closed furnace at high temperatures followed by wet impregnation procedure (suspension of Fe(NO$_3$)$_3$ in ethanol) [9]. Iron-doped TiO$_2$ materials were prepared by a microwave-assisted method. Regardless of the nanometric nature of the materials, crystalline structure, and high surface area, the photocatalytic activity was very low [10].

Besides the modification of absorption properties, it is also well known that the catalytic properties of titania can be tuned by modification of its crystal structure, morphology, surface properties, and size. A chemical approach in the preparation of transition metal-doped TiO$_2$ allows fine tuning of the TiO$_2$ properties by varying the synthesis conditions. In the current work, Fe^{3+}-doped TiO$_2$ nanopowders with different iron contents prepared with a sol–gel method were characterized using spectroscopic and microscopic techniques, in order to elucidate their composition, size, and crystalline phase. Our selection of Fe^{3+} as dopant was based on previous reports that indicate that small amounts of iron cation enhance the photocatalytic activity of TiO$_2$ by acting both as hole and electron traps [11]. Also, Fe^{3+} ionic radii (69.0 pm) are slightly smaller than that of Ti^{4+} (74.5 pm), which permits to incorporate the iron ion into the TiO$_2$ lattice, rendering a narrowing in the forbidden band gap of the TiO$_2$. The visible light photocatalytic activity of these materials was evaluated for the degradation of methyl orange (MO) and methylene blue (MB) in aqueous solution. The influences of several variables such as amount of catalyst, hydrogen peroxide concentration, and initial pH of the solution on the efficiency of the photocatalytic reaction were experimentally tested.

Mexico as many other countries will face scarcity water problems; therefore, the implementation of water treatment technologies that assure safe consumption of recycled water is pragmatically important. With this fact in mind, we are interested in the industrial application (tertiary

treatment of industrial and hospital effluents) of the photocatalytic process presented. In the last decade, new toxicology testing assays have been developed in order to evaluate toxicity (cytotoxicity, oxidative stress, hemolytic activity, and DNA damage) of nanomaterials [12–14]. In vitro systems are used to rapidly and inexpensively predict the effects of nanomaterials at the cellular level. Regardless of the many publications involving iron-doped TiO_2 materials, most of the reports lack the toxicological evaluation and practical large scale application. In order to attain large scale production, a practical, simple, and economic approach for the development of visible light active photocatalyst should be implemented. In this work, we report on the green production, characterization, and toxicological (in vitro toxicity of the materials was evaluated using human red blood cells) evaluation of visible light active Fe^{+3}–TiO_2 materials. Our results clearly demonstrate the variation on the physicochemical properties and photocatalytic activity of the materials, resulting from the level of iron doping within the material. Due to the low sintering temperature ($\sim$400 °C) used, the materials show small crystallite sizes, high surface areas, and good photocatalytic activity under visible light. Further studies will be directed to the fabrication of supported iron-doped materials, using as starting materials the optimized catalyst reported in this work. Supported materials will facilitate the large implementation of the catalyst for the tertiary treatment of hospital effluents. It is well known that solar-assisted photocatalytic process depends upon climatic conditions. Light emitting diodes (LEDs) are considered as a cheap and reliable source of energy (due to higher efficiency in light-electricity conversion), which replace the use of UV lamps in many applications and can also contribute to reduce the time and cost of treatment of effluents on cloudy days. In this work, a home-made LEDs-activated reactor was employed to determine the photocatalytic activity of the prepared materials.

Experimental procedures

(A) *Synthesis of TiO_2–Fe^{3+}* Colloidal solutions of TiO_2–Fe^{3+} nanoparticles were synthesized by optimization of sol–gel process conditions. Different amounts of $Fe(NO_3)_3 \cdot 9H_2O$ (in order to prepare materials with an Fe^{3+}/TiO_2 mol ratio = 0.01, 0.03 and 0.05) were dissolved in 20 mL of glacial acetic acid. Titanium(IV) isopropoxide (10 mL, 0.033 mol) was slowly added to glacial acetic acid–Fe^{3+} solutions with continuous stirring. Arabic gum (0.9 g) was dissolved in 30 mL of double distilled water, and the mixture was heated to 60 °C for 30 min. Arabic gum aqueous solution was cooled to room temperature

and then was drop wisely added to titanium-Fe^{3+} solution under vigorous stirring. The resulting solution was stirred for 8 h and allowed to dry at 100 °C, after which it was calcined at 400 °C in air for 4 h.

(B) *UV–Visible and diffuse reflectance characterization* The absorption spectra of TiO_2–Fe^{3+} colloidal suspensions were obtained with a Thermo scientific Helios Omega UV–Vis spectrophotometer. The technical variables of operation were ambient temperature, scanning range of 300–600 nm, and 0.5 mL of colloidal suspension diluted to 5 mL.

A Thermo Fisher Scientific-Evolution 300 instrument equipped with an integrating sphere (TFS-Praying Mantis) for diffuse reflectance measurements of the powders was used to establish the optical band gap. A $BaSO_4$ sample was analyzed as a reference.

(C) *X-ray powder diffraction (XRD)* The powder XRD patterns of the samples were recorded in a Siemens D-5000 Diffractometer using Cu K_α radiation ($\lambda = 1.5418$ Å) at a scanning rate of 0.05°/min for 2θ ranging from 10° to 85°.

(D) *Specific surface area (SSA) determination* The specific surface area of the catalysts was determined from nitrogen adsorption and desorption isotherms at 77 K using a Quantachrome Autosorb-1 instrument. Prior to the measurement, all catalysts were degassed with nitrogen at 200 °C under vacuum for 10 h and backfilled with helium gas to remove excessive moisture or adsorbed contaminants on the materials surface.

(E) *Raman characterization* Raman spectra of bare and doped TiO_2 samples were obtained with a micro-Raman system using He–Ne laser (632.8 nm) and 10 mW of power at the sample. Raman spectra were recorded with a monochromator equipped with an air-cooled CCD camera as detector. Microsampling was accomplished with a Zeiss 40× objective with a numerical aperture of 0.75. With this objective, the laser beam focal point diameter was ca. 2 μm. Characteristic peaks for anatase were determined comparing their relative positions with previous reports.

(F) *Microstructural and elemental analysis* The morphology and elemental composition of the nanomaterials were determined using a Tecnai F20-G^2 transmission electron microscope (TEM) (FEI Company, Hillsboro, Oregon) with electron diffraction (ED) and X-ray energy dispersive spectroscopy (EDS) capabilities in order to obtain nanostructural information, crystalline phase, and elemental composition. An atomic-resolved lattice fringe of the materials was characterized by high resolution TEM

Table 1 Summary of the amounts of TiO_2–Fe^{+3} (1, 3, and 5 mol%) tested on the evaluation of toxicity toward HRBC

Tube	1	2	3	4	5	6	7	8	9	10
Amount of NMs (mg)	1	2	3	4	5	6	7	8	9	10
Concentration (mg/mL)	0.1	0.2	0.3	0.4	0.5	0.6	0.7	0.8	0.9	1.0

(HRTEM) with a Tecnai F20-T operating at 200 kV and equipped with slow scan cooled CCD (Gatan) camera with the digital micrograph software, with resolution of 1 mega pixel. The digital micrograph software provided processing and quantification of the images, and gave an opportunity to perform the phase analysis in nanoscale during the HRTEM real time investigation. The HRTEM images were taken at a direct magnification of 600 thousand magnitudes with the point resolution of 0.2 nm. The samples were dispersed in absolute ethanol and deposited onto the carbon-coated copper grid. An axis ULTRA XPS (Kratos Analytical Inc., New York, USA) was employed to determine the elemental composition of TiO_2–Fe^{3+} materials. The excitation source was the K_α radiation of an aluminum anode. Further details of the measurements are described elsewhere [15].

(G) *Photocatalytic degradation studies* The photocatalytic activities of the prepared TiO_2–Fe^{3+} powders were studied by degradation experiments using MO and MB as model compounds. 150 mL of dye solutions were used and treated with 150 mg of TiO_2–Fe^{3+} powders. Pure TiO_2 powder was also tested under same conditions for comparison.

Experiments were carried out using a magnetically stirred tubular reactor and visible light (the reactor contains three LEDs lamps, LED bulb light, WBH-BL-001, 3W,) at room temperature and continuous air bubbling. The initial concentration of the dyes was fixed at 20 mg/L. The pH of the suspension was adjusted either with 0.1 M HCl or 0.1 M NaOH. After experimental evaluation, the optimum pH value was found to be 2.5 for MO and 9.5 for MB degradation. 60-min adsorption time in dark condition was allowed before the photoreactions. Aqueous solutions of dyes were illuminated in the presence of air, H_2O_2, and TiO_2–Fe^{3+} (different concentrations of H_2O_2 were evaluated). The evolution of the photocatalytic degradation was measured by means of UV–Vis spectroscopy. Samples (5 mL) of the suspension were withdrawn after a fixed (1 h) time interval. The pH of the sample was adjusted (from 9.5 to 7) in order to desorb the unreacted dye from the surface of the catalyst; then, the catalyst was removed by centrifugation at 4000 rpm for 10 min. The supernatants were analyzed for residual dyes concentration using a spectrophotometer (UV–Vis Helios Omega, Thermo

Scientific) at 660 nm for MB and 466 nm for MO. Iron leaching was measured by means of Atomic Absorption Spectroscopy (AAS, AAnalyst 800, Perkin Elmer).

(H) *Toxicity studies* In vitro toxicity studies were carried out using freshly purified erythrocytes and human whole blood. Heparin-stabilized human blood was freshly collected. Physiological saline solution (PSS) was added to test tubes (10 mL of PSS in each tube). Different amounts of nanomaterials (NMs) were added to each tube according to Table 1.

A 50 μL sample of whole blood was added to each tube. All samples were prepared in triplicate, and the suspension was briefly vortexed before leaving at static conditions at room temperature for 24 h. Four series of tubes were prepared. One assay was conducted under illumination and the other in the dark. The temperature of the assays was varied: 37 and room temperature (24 °C). After that, the mixtures were centrifuged at 1500 rpm for 10 min. The amount of hemoglobin was determined by UV–Vis spectroscopy and measured with the reference wavelength of 525 nm. For the assays involving erythrocytes, blood samples were centrifuged at 4000 rpm for 10 min. The cellular package was separated and washed three times with PSS. 1:5 dilutions of erythrocytes were prepared using PSS. Hemolytic activity assays were conducted as described for the whole blood study.

Results and discussion

Optimization of TiO_2–Fe^{3+} synthesis

In this work, TiO_2–Fe^{3+} and TiO_2 nano-structured powders were synthesized using a green, environmentally friendly, acid-catalyzed sol–gel technique. The sol–gel method was explored because this approach easily allows for the tailoring of specific features of nano-structured materials. In turn, this is due to the fact that it permits for the combination of reagents at molecular level during sol formation [16]. Particularly, iron cations were introduced in the initial solution, before gellification, what promotes their lattice incorporation. One of the serious problems encountered in colloidal sols is the strong aggregation of particles during the sol–gel transition. In order to avoid agglomeration,

Fig. 1 a Synthesis of colloidal suspensions of TiO_2–Fe^{3+} using Arabic gum as surfactant. b Colloidal suspensions of TiO_2–Fe^{+3} at different metal ion (Fe^{+3}) concentration (left). Nanopowders of TiO_2–Fe^{+3}. From left to right, TiO_2–Fe^{+3} (1 %), TiO_2–Fe^{+3} (3 %), and TiO_2–Fe^{+3} (5 %). The image clearly shows that as the Fe ion concentration increases, the yellow color of the powders increases (Color figure online)
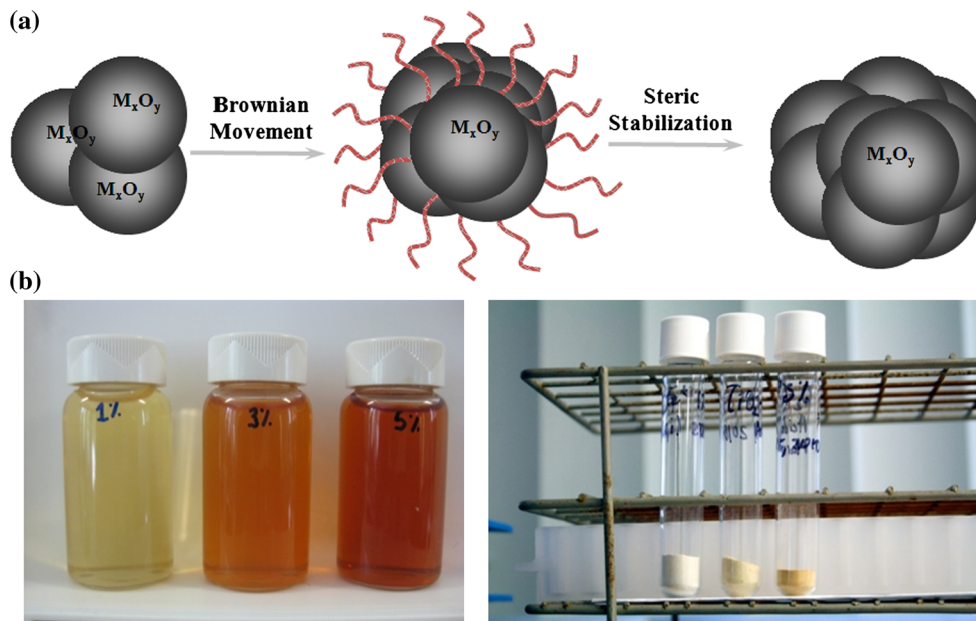
surface-controlling agents are commonly used, such as complex-forming agents (i.e., β-diketonates), amines, phosphines, or chelating agents. Although the use of chemical surfactants allows for the production of materials with very uniform particle sizes in the nanometer range, some drawbacks accompany its use: cost, toxicity, and the need of elevated temperatures to remove them. In order to avoid the aforementioned problems, Arabic gum (a widely used biopolymer in the food industry) was employed as bio-emulsifier. Besides the low cost and lack of toxicity of the polymer, it allows a fine control on the size distribution of the particles, can be removed at low temperatures and facilitates the production of coatings (adheres easily to different substrates).

In our synthesis, the amount of Fe ion was varied as 1, 3, and 5 mol%, respectively. The resulting colloidal solutions are stable for months due to steric stabilization by the dispersing agent (Fig. 1a). It is observed that as the amount of Fe ion increases, the color intensity of the solution and powders increases (Fig. 1b), indicating that the prepared materials are visible light sensitive. It has been reported that the solubility limit of iron in anatase is about 1 atom% [6, 17]. Taking into consideration this solubility limit, 3 and 5 % of iron-doped materials exceed the amount of iron that can be incorporated into the TiO_2 lattice resulting in segregation of iron oxides to the surface of the materials. The literature reports show controversies regarding the optimal experimentally determined amount of iron doping able to enhance photocatalytic activity. Zhang et al. [18] proposed that the optimal doping ratio is dependent not only on the nature of the doping atom but also on the morphology and the size of the particles. Bloh and
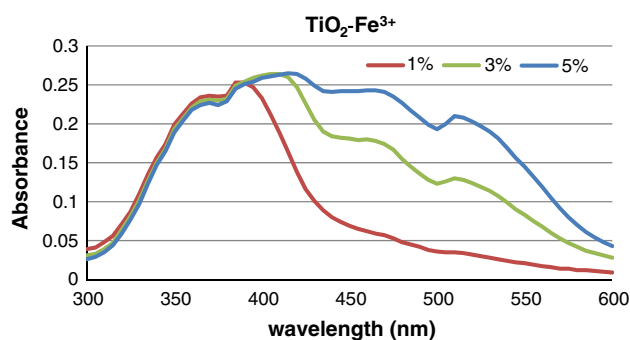

Fig. 2 UV–Vis spectra of colloidal solutions of TiO_2–Fe^{3+}. The red shift of the absorption properties of the suspensions is clearly illustrated as the amount of iron doping increases (Color figure online)

co-workers developed a mathematical model in order to explain the complex relationship between doping ratio and particle size. Applying the model, it is found that in order to achieve the optimal doping ratio, it is required to have at least one dopant atom per particle and, on the other hand, not too many dopant atoms per particle to avoid recombination centers [17]. The small size (~9 nm) of the iron-doped TiO_2 materials reported in this work allows for doping up to 1 %.

UV–Vis and diffuse reflectance characterization

The absorption properties of the colloidal suspensions were analyzed by UV–Vis spectroscopy (Fig. 2). Our results indicate that UV–Vis spectra of iron-doped nanomaterials are red shifted, corroborating the modification (decrease) of
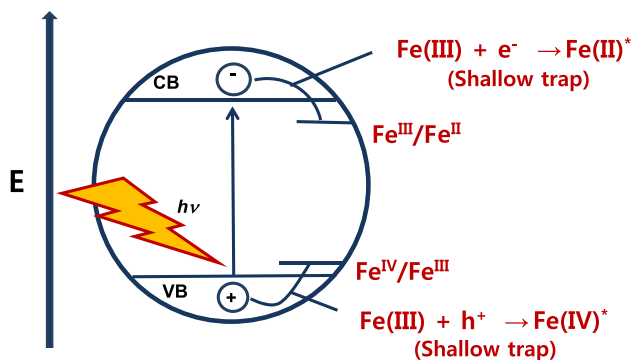
Fig. 3 Schematic diagram for Fe^{3+} mediating interfacial charge transfer in doped TiO_2

Fig. 4 UV–Vis diffuse reflectance spectra of iron-doped and bare titanium dioxide materials

the forbidden band gap of the produced photocatalysts. The maximum absorption peak for the $TiO_2–Fe^{3+}$ (5 %) was found to be 415 nm versus the one encountered for $TiO_2–Fe^{3+}$ (1 %), which is 390 nm. The spectra also show an increase of absorptive properties at 470 and 520 nm as the amount of doping increases. Our results evince that the presence of iron renders absorption in the visible region, it is also easily inferred that the absorption is directly influenced by the amount of iron doping in the samples, observing a more pronounced red shift as the percentage of iron content in the samples increases.

Absorption in the visible region can be attributed to the excitation of 3d electrons of Fe^{3+} to the TiO_2 conduction band (Fig. 3). Zhang and co-workers have reported that in the metal ion-implanted TiO_2, the overlap of the conduction band due to Ti (d orbital) of TiO_2 and the metal (d orbital) orbital of the implanted metal ions could decrease the band gap of TiO_2 to absorb the visible light [19]. Besides the red shift in the absorption properties of the iron-doped TiO_2 materials, presented in this work, the formation of new states close to the valance band and conduction band of TiO_2 can contribute to an enhanced photoactivity (decreased e^-/h^+ recombination) of the above-mentioned materials (Fig. 3).

Figure 4 shows the UV–Vis spectra of the undoped (TiO_2) and the doped ($TiO_2–Fe^{3+}$) samples. It can be clearly observed that the band edge of doped materials shifts to the visible region (in accordance to the UV–Vis absorption shown by colloidal solutions). The band edge for the undoped TiO_2 sample (prepared using the same experimental protocol to prepare iron-doped TiO_2) appears at about 403 nm, while the band edges of the iron-doped TiO_2 samples shifted to longer wavelength regions with higher absorption intensity after Fe^{3+} doping (1 %). The light absorption extended to the highest value of 548.7 as Fe^{3+} doping was increased to 5 mol%. The Kubelka–Munk
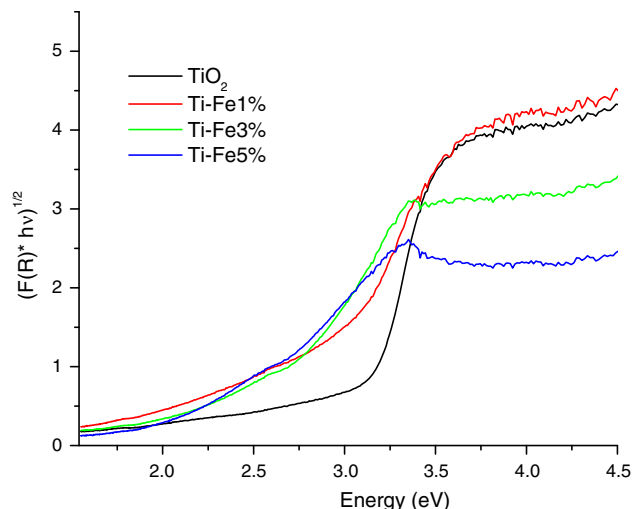
theory is generally used for analyzing the diffuse reflectance spectra obtained from weakly absorbing samples. The band gap of bare and Fe^{3+}-doped TiO_2 samples was calculated by the Kubelka–Munk function based on the following equation:

$$F(R) = \frac{(1 - R)^2}{2R},$$

where R is the absolute reflectance of the sample and $F(R)$ is proportional to the extinction coefficient (α). The basic Kubelka–Munk model assumes the diffuse illumination of the particulate coating.

A modified Kubelka–Munk function can be obtained by multiplying the F(R) function by $h\nu$ using the corresponding coefficient (n) associated with an electronic transition as follows: $(F(R) * h\nu)^n$ [20], where n is a constant which determines the type of optical transitions, for TiO_2, $n = 1/2$ for direct allowed transition. Regarding the E_g values, it was found that as the amount of Fe^{3+} increases from 0 to 5 mol%, the band-gap energies decreased in the range of 3.08–2.26 eV as shown in Fig. 4 and presented in Table 2. It has been reported that iron doping could form a dopant energy level above the valence band of TiO_2 (Fe^{4+}/Fe^{3+} redox pair). The energy level of Fe^{3+}/Fe^{2+} lies below the conduction band level of TiO_2. As a consequence of the introduction of new energy states, doping of TiO_2 with Fe^{3+} ions induce band edge bending (charge-pair generation: $Fe^{3+} \rightarrow Fe^{4+}$; $Fe^{3+} \rightarrow Fe^{2+}$) and reduces rate of recombination (charge trapping and recombination), rendering visible light activity in iron-loaded samples [7]. Electrons that are excited from the valence band of TiO_2 by absorbing visible light energy will be captured by an interband trap site formed by the

Table 2 Details of the physicochemical properties of the bare TiO_2 and TiO_2–Fe^{+3} nano-structured powders

Catalyst	XRD crystalline phase	Crystallite size (nm)[a]	E_g (mV)	SSA (m^2/g)
TiO_2	Anatase	12.69	3.08	110.7
TiO_2–Fe 1 %	Anatase	8.95	2.71	177.3
TiO_2–Fe 3 %	Anatase	8.29	2.47	167.6
TiO_2–Fe 5 %	Anatase	9.52	2.26	165.8

[a] Particle size was calculated with Scherrer equation using the 101 diffraction peak of anatase

substitution of Fe^{3+} for Ti^{4+} [21]. As a result, enhanced photocatalytic activity is encountered in iron-doped titanium dioxide materials.

X-ray powder diffraction

XRD measurements were performed to identify the crystalline phases synthesized by the sol–gel process at calcination temperature of 400 °C and iron concentrations of 1, 3, and 5 mol%, respectively. Figure 5 shows the analysis of the different samples. The XRD patterns of the samples show that the major crystalline phase detected in all samples is anatase, without significant difference in comparison with the undoped TiO_2 sample. No characteristic peaks of rutile phase or brookite phase are revealed, which means that Fe^{3+} doping can maintain metastable anatase phase of TiO_2 [22]. Additionally, no characteristic peaks were detected for Fe or any impurities. The absence of the diffraction peaks of Fe_2O_3 may be justified since the amount of doped Fe^{3+} is so low that it cannot be detected by XRD. The diffraction peaks are remarkably broadened. The average crystallite sizes of the bare and Fe^{3+}-doped materials were calculated according to the Scherrer's equation (Table 2). The crystallites are very small: 12.69 nm (TiO_2), 8.95 nm (TiO_2–Fe^{3+} 1 %), 8.29 nm (TiO_2–Fe^{3+} 3 %), and 9.52 nm (TiO_2–Fe^{3+} 5 %). It is observed that the crystallite size of the materials decreases from 8.95 to 8.29 when the iron ions content increases (from 1 to 3 %). Such an inhibition of the crystallographic domain growth due to the presence of transition metals inside the TiO_2 lattice is well documented in previous works [23]. In the case of TiO_2–Fe^{3+} 5 %, the crystallite size increases slightly, suggesting that solubility limit was reached, and excessive amount of iron was segregated to the surface of the material in the form of oxide. The lattice constants "a" and "c" for anatase ($a = b \neq c$) crystal system were determined from the two appropriate reflections, (101) and (200), using Eq. 1. From Table 3, we can see the variation on lattice constants as a function of Fe

doping; the modification on the lattice parameters indicates incorporation of Fe into the lattice.

$$\frac{1}{d} = \frac{(h^2 + K^2)}{a^2} + \frac{l^2}{c^2}, \tag{1}$$

where d is the lattice spacing, determined by Bragg's law in Eq 2.

$$n\lambda = 2d \sin \theta. \tag{2}$$

It is important to remark that all lattice parameters encountered for bare and doped TiO_2 materials presented in this manuscript are smaller than the reference (PDF 01-086-1157) material due to the very fine size particle. The proposed sol–gel method allows fine tuning on the size of the material, high crystallinity (only anatase), and incorporation of Fe ions into the TiO_2 lattice. One of the main advantages of the XRD technique is that it provides meaningful ensemble-averaged information about both medium range, and local, atomic structure in nanosystems. By characterizing the sample as a whole, this technique is an essential complement to HRTEM which provides rather detailed information on only a few particles.

The HRTEM analysis of the samples corroborates that the small grain size ($\sim$9 nm) of the materials is responsible from the broadening of diffraction peaks. HRTEM examination shows the high crystallinity of the iron-loaded TiO_2 nanoparticles. From XRD analysis, we can clearly see the effects on the lattice parameters of the materials upon iron doping (Table 3; Fig. S5).

SSA determination

The specific surface areas of bare and iron-doped catalyst were determined and reported in Table 2. Our catalysts present high specific surface areas, the highest value corresponds to TiO_2–Fe^{+3} 1 % (177.3 m^2/g), followed by TiO_2–Fe^{+3} 3 % (167.6 m^2/g), TiO_2–Fe^{+3} 5 % (165.8 m^2/g), and TiO_2 (110.7 m^2/g). As we compare our results with the previously published ones, we can observe that our materials exhibit higher surface areas; for instance, Wang et al. [24] prepared Fe^{3+}–TiO_2 by plasma oxidative pyrolysis. It was encountered that 1, 3, and 5 % iron-doped materials exhibited SSA values of 30.2, 25.3, and 21 m^2/g, respectively. Another example reports SSA values of 58, 56, and 53 m^2/g for 1, 2, and 5 % iron-doped materials [25]. The small particle size and large specific surface areas encountered in our materials lead to an increase in the number of available surface active sites, which consequently results in a higher interfacial charge carrier transfer rate for photocatalysis and increased photocatalytic efficiency.

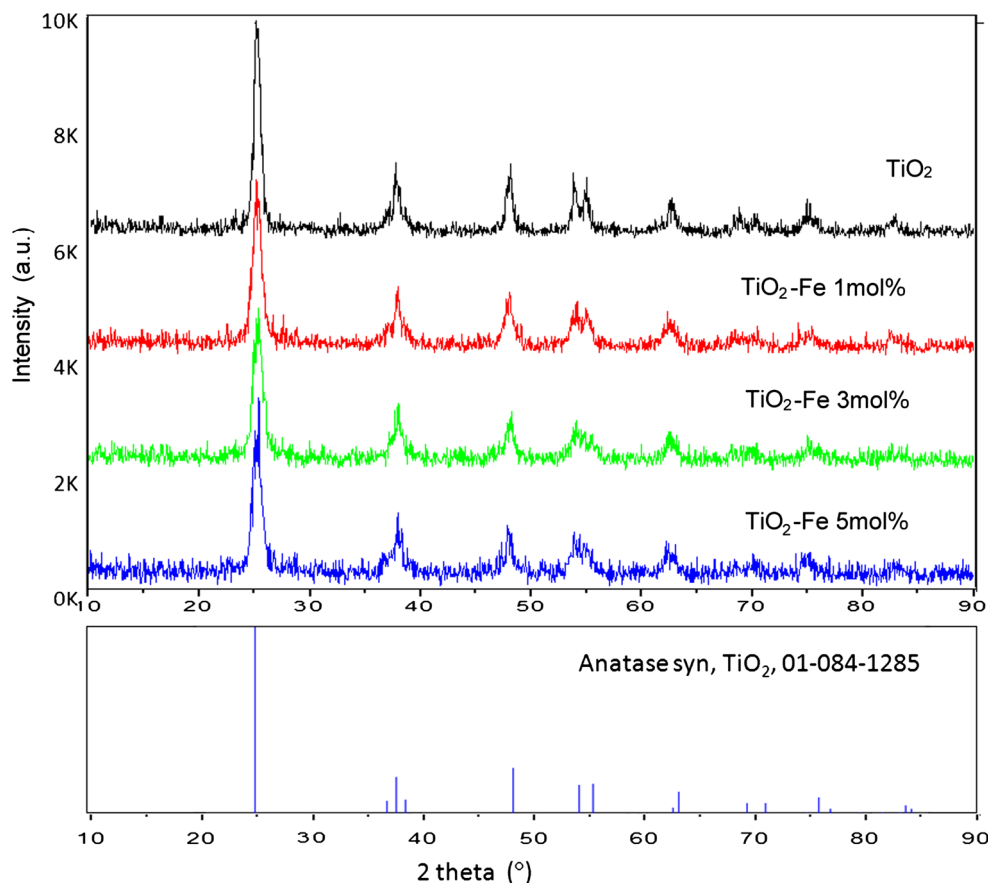**Fig. 5** XRD diffraction patterns of iron-doped and bare titanium dioxide powders

Table 3 The nominal atomic composition, mean crystallite size, and anatase lattice parameters obtained from XRD

% Fe	D (nm)	$a = b$ (Å)	c (Å)	V (Å^3)
0	12.69	3.776	9.367	133.5
1	8.95	3.780	9.442	134.9
3	8.29	3.770	9.241	131.3
5	9.52	3.767	9.251	131.3

Raman analyses

The Raman spectra of the samples confirm the presence of the anatase form of titania in all the materials. For P25-TiO$_2$, it has been reported that due to overlapping of A$_{1g}$ and B$_{1g}$ bands, the Raman spectrum of the material shows only five vibrational bands at 140, 188, 388, 507, and 631 cm^{-1} [26]. Our results are illustrated in Fig. 6. We can clearly see that the vibrational peaks reveal a slight red shift: 142, 193, 393, 515, and 640 cm^{-1}, compared to P25-TiO$_2$ materials. The absence of the characteristic vibrational bands at 225, 247, 299, 412, 497, and 613 cm^{-1}, which correspond to the α-Fe$_2$O$_3$ material, or the resonances at 350, 500, and 700 cm^{-1} characteristic of γ-Fe$_2$O$_3$ material, suggest no formation of iron oxides.
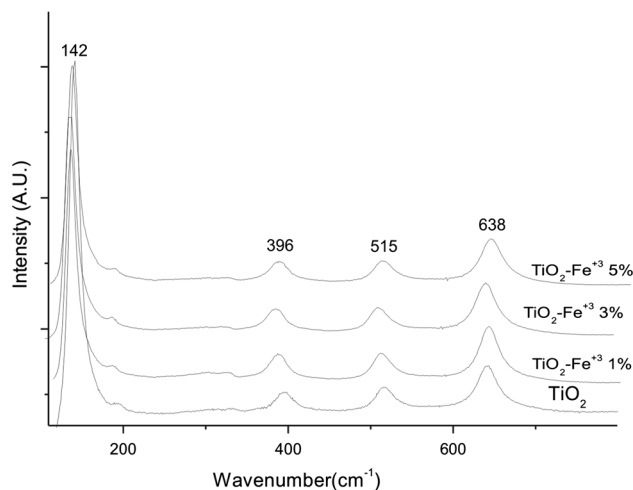

Fig. 6 Raman spectra of bare and iron-doped titanium dioxide powders

Based on these results, we can also discuss that in the material it will be difficult to detect the trace amounts of iron oxides materials (assuming they are present) due to the small portion of iron (1, 3, and 5 %). These results are in accordance with the results encountered by XRD and HRTEM analysis.

Fig. 7 a HRTEM image of bare TiO_2. The image revealing the (101) lattice fringes (3.60 Å) also showed clearly the highly crystalline nature of the nanoparticles. **b** SAED of bare TiO_2 we find that [101] = 3.49 Å, [004] = 2.38 Å, [200] = 1.87 Å, [105] = 1.71 Å. **c** HRTEM Image of 5 % Fe^{3+} TiO_2. The image revealing the (101) lattice fringes (3.56 Å) also showed clearly the highly crystalline nature of the nanoparticles. **d** SAED of 5 % Fe^{3+} TiO_2 we find that [101] = 3.51 Å, [004] = 2.37 Å, [200] = 1.83 Å, [107] = 1.26 Å
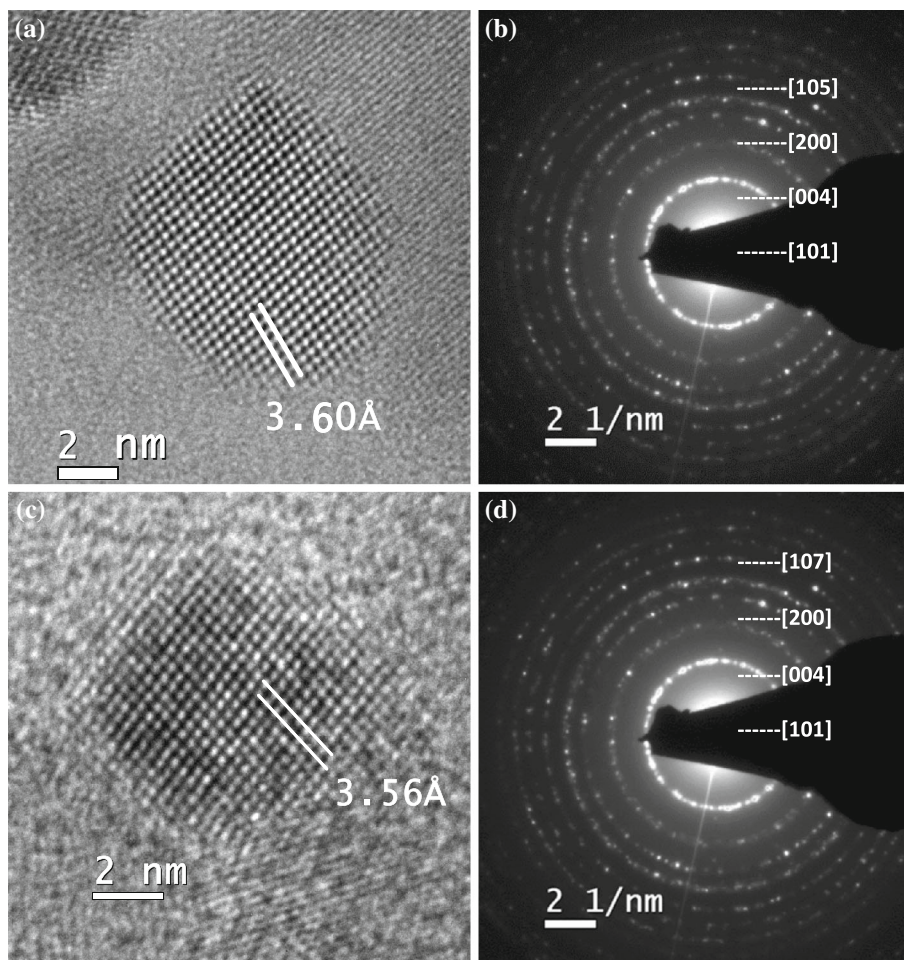
Microstructural and elemental analyses

The high resolution transmission electron microscopy (HRTEM) analysis indicated the presence of uniformly distributed particles with average particle size of about 9 nm. (The average size particle was calculated using Image J program analysis from HRTEM images presented in supplementary information.) The HRTEM analysis of TiO_2 and TiO_2–Fe^{3+} 5 % materials is illustrated in Fig. 7a, b. The images illustrate the differences in the (101) lattice fringes encountered for TiO_2 (3.60 Å) and 5 % iron-doped TiO_2 (3.56 Å) materials. The images also show the highly crystalline nature of the nanoparticles. Selected area electron diffraction (SAED) patterns are presented in Fig. 7c, d. According to the HRTEM lattice fringes, ring pattern, and SAED pattern, the crystalline part of the samples consists of *anatase* (PDF 01-086-1157 with the lattice constant of 3.7852 × 9.5139 Å and 90°) as dominant phase. All rings are indexed to anatase phase, for TiO_2 [0.349 nm (101), 0.238 nm (004), 0.187 nm (200), and 0.171 nm (105),] and [0.351 nm (101), 0.237 nm (004), 0.183 nm (200), and 0.126 nm (107)] for TiO_2–Fe^{3+}-5 %,

without any additional diffraction rings of secondary phases which confirm the purity of the sample. It is hardly possible to identify the difference between Fe metal and Fe^{3+} ion from the d-space. Therefore, X-ray photoelectron spectroscopy (XPS) was applied to determine the oxidation state of iron. It was found that the XPS provides evidence for Fe^{3+} surface species in the Fe^{3+}–TiO_2 composite. The Fe 2p XPS spectrum of TiO_2–Fe^{3+} materials is shown in Fig. 8. The line shape and binding energies in the doped materials match those of Fe_2O_3 in accordance with previously presented results by Mangham et al. [27]. It should be noted that XPS technique measures the elemental composition only for the surface layer; thus, segregated iron ions are going to be encountered in the form of iron oxides. There is no evidence of Fe^{2+} in the synthesized iron-doped materials [28]. It is difficult to unify the results encountered for the Fe $2p_{3/2}$ spectrum, since the peaks are influenced by ligand field effects due to the Fe environment (i.e., tetrahedral, octahedral), crystalline disorder at the nanoparticle surface, and Russell–Saunders coupling of Fe(III) [29]. Also, one needs to keep in mind that XPS data are not perfectly homogeneous because of the intrinsic
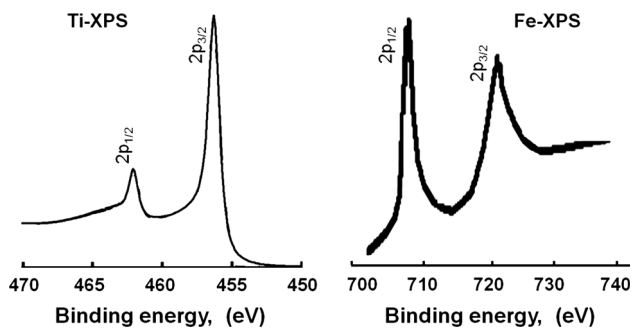
Fig. 8 The XPS spectra of Ti 2p and Fe 2p of TiO_2–Fe^{+3} materials

inhomogeneity of the atoms and their immediate chemical environment within each nanoparticle. Taking into consideration the theoretical and experimental results, we can argue that the Fe 2p XPS spectra for iron-doped TiO_2 materials can be ascribed to Fe^{3+} ions. There are not significant differences among the spectrum of each individual synthesized (1, 3, and 5 %) material since the variation in the amount of iron doping is low. The Fe element in the samples exists mainly in the +3 oxidation state because $Fe(NO_3)_3$ was used as iron precursor.

The elemental composition of the nano-structured materials was elucidated by EDAX analysis. EDAX analysis was performed in all the samples. Results are summarized in Table 4. Our data indicate that the samples are pure since they only contain Ti, O, and Fe. The incorporation of iron ions within the material is lower than the percentage established in the preparation protocol. From the table, we can see that the amount of iron incorporated in the materials is 0.45 (established 1 %), 0.96 (established 3 %), and 1.61 (established 5 %). Taking into consideration the photocatalytic activity of the presented materials, their composition, and physicochemical properties, we can conclude that the synthetic method developed in this work allows for the preparation of ultrafine particles of bare and

Fe-doped TiO_2 materials. The materials have a uniform size distribution, large surface areas, and iron ions immersed into the TiO_2 lattice. All these properties render good photocatalytic activity under visible light.

Degradation of the dyes

The photocatalytic degradation of MO and MB was performed using TiO_2–Fe^{3+} as a catalyst and visible light for activation. Several parameters (pH, H_2O_2 concentration, time of reaction, amount of catalyst) were optimized in order to perform the photocatalytic degradation of MO and MB. To exclude the possibility that dye degradation was caused by light radiation and/or H_2O_2, we did blank experiments where only dye solutions in the absence of the catalysts were radiated with visible light in the presence of H_2O_2. The dye solutions were saturated by oxygen (air) before processing. UV–Vis spectroscopic analysis performed at different intervals during the photocatalytic degradation allowed to follow the chemical evolution of the solution. Figure 9 shows the rapid decay of the MO concentration in the aqueous solution.

In heterogeneous photocatalytic process, the first step for the degradation of pollutants is their adsorption to the surface of the catalyst. Pollutants will adsorb easily if appropriate electrostatic interactions are developed within the surface of the catalyst. Methylene blue presents a cationic configuration in alkaline solution; at the same time, it was reported that the point of zero charge (PZC) of iron-doped TiO_2 materials oscillates between 7.2 (TiO_2/Fe/0.3) to 8.1 (TiO_2/Fe/5). Therefore, at pH values higher than the PZC, the surface of the material becomes negatively charged; since MB has a cationic configuration, its adsorption is favored in alkaline solution [25, 30].

In the case of MO, the dye degradation is more efficient in acidic medium (pH 3.5) due to the better sensibility of the protonated form of the dye for oxidation process [31]

Table 4 EDAX analysis to determine the chemical composition of bare TiO_2 and iron-doped TiO_2 materials

Material	Element	Wt%	At.%	K ratio	Z	A	F
TiO_2	O K	40.98	67.52	0.0446	1.0921	0.997	1.0000
	Ti K	59.02	32.48	0.5538	0.9259	1.0133	1.0000
TiO_2–Fe^{3+} 1 %	O K	38.05	64.82	0.0459	1.1023	0.1095	1.0000
	Ti K	61.02	34.72	0.5706	0.9266	1.0086	1.0000
	Fe K	0.93	0.45	0.0080	0.9194	0.9373	1.0000
TiO_2–Fe^{3+} 3 %	O K	41.32	67.93	0.0530	1.0960	0.1170	1.0000
	Ti K	56.54	31.11	0.5270	0.9210	1.0089	1.0000
	Fe K	2.04	0.96	0.0176	0.9137	0.9429	1.0000
TiO_2–Fe^{3+} 5 %	O K	40.65	67.40	0.0525	1.0973	0.1178	1.0001
	Ti K	55.97	31.00	0.5215	0.9222	1.0083	1.0021
	Fe K	3.39	1.61	0.0292	0.9149	0.9434	1.0000

Fig. 9 Photocatalytic degradation of MO under visible light (LEDs). Bare TiO_2 and iron-doped TiO_2 materials
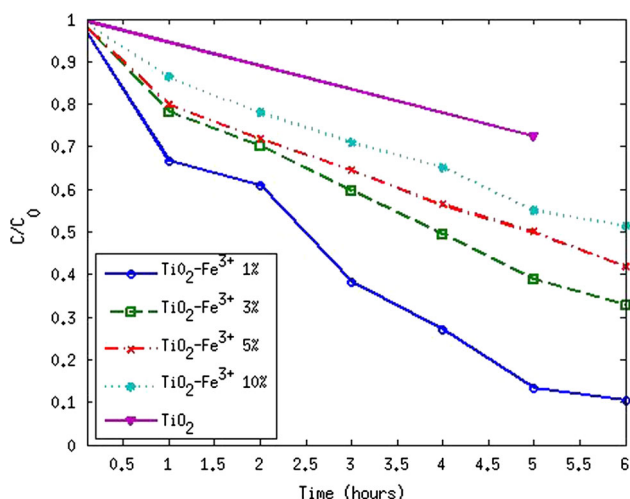

Fig. 10 Photocatalytic degradation of MB under visible light (LEDs). Bare TiO_2 and iron-doped TiO_2 materials

and to the adsorption of the protonated form of the dye onto the surface of the catalyst. Dai et al. [32] elucidated the mechanism of MO degradation using mesoporous titania nanoparticles. Different pH values were evaluated (1.5, 2.0, 3.0, and 5.0). The kinetics for the degradation of MO was evaluated as a function of the pH. The largest rate constant was observed to be for pH 2.0 which indicates that the best photocatalytic efficiency can be obtained under those acidic conditions. In this work, the photocatalytic degradation of MO was also performed at neutral and basic pH (9.5) for comparison. Our results showed that no degradation occurred at these pH values even after 7 h of photocatalytic reaction.

The amount of catalyst employed was also optimized. Different amounts (50, 100, 150, and 200 mg of catalyst/ 150 mL of dye solution) of catalyst were evaluated in order to perform the experiment. Our results indicate that 1 mg of catalyst/mL of solution facilitates the reaction, removing the dye relatively faster compared to lower amount of catalyst. It was also observed that higher concentrations of catalyst inhibit the photocatalytic degradation since light cannot penetrate the solution easily. Also, the removal of the catalyst at higher concentrations becomes cumbersome. The optimized concentration of H_2O_2 for the removal of MO was found to be 150 ppm (50 and 100 ppm were also evaluated) (Fig. 10).

From Fig. 9, we observe that the degradation percentage for MO is higher for TiO_2–Fe^{3+} 1 % when the amount of H_2O_2 is 50 ppm using LED reactor. It was also observed that the reproducibility and efficiency of the experiment are uniform for all the tested materials. Our results are in accordance with some previous reports related to this work [33].
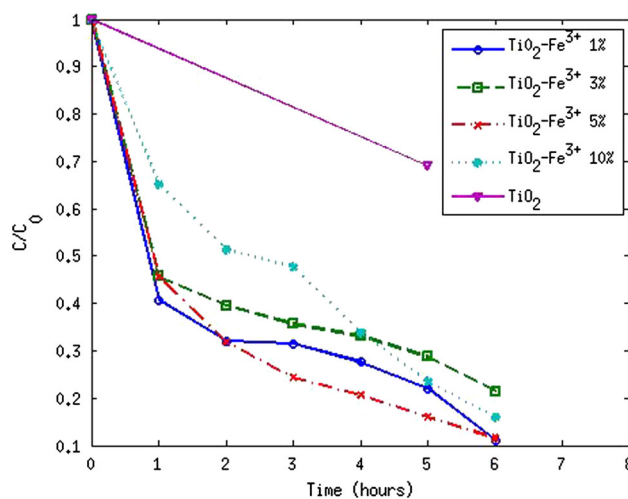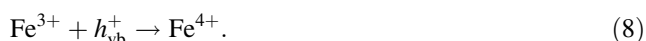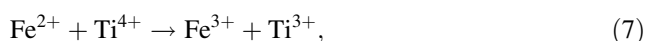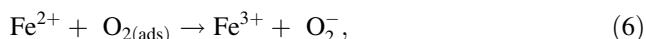
In order to attain an improvement in the photoactivity of iron-doped TiO_2 materials, optimal iron doping should be achieved, which are mainly dependent on the size of the materials [17, 34]. Several groups have indicated that the optimal iron doping is about 0.5 mol % [35]. In our study, we evaluated photocatalyst with Ti/Fe mol ratios of 1, 3, and 5 %. We observe visible light response and good photocatalytic activity of the aforementioned materials on the degradation of MO and MB dyes. In order to justify our observations, leaching of iron ions into solution was evaluated by means of atomic absorption spectroscopy. It was encountered that in average the photo-bleaching of iron is 0.6695, 0.6505, and 0.968 ppm for 1, 3, and 5 % irondoped titanium dioxide materials. We believe that the enhanced photoactivity of these materials relates to a synergistic mechanism that encompasses heterogeneous photocatalysis mediated by TiO_2–Fe^{3+} materials and Foto-Fenton like process due to the presence of homogeneous Fe^{3+} catalyst and acidic media [11].

Methylene blue was photo-degraded using visible light and iron-doped titanium dioxide catalyst (Fig. 10). We observe that the rate of degradation was significantly influenced by the amount of H_2O_2 used as coadyuvant in the process. We do not observe a marked difference on the performance of the doped materials for the degradation of MB. Sadik [36] reported an increase in the decolourization rate of aqueous solutions of acid orange 7 when H_2O_2 was added to the system. It was postulated that the enhancement of the rate of dye decolourization using UV/TiO_2/ H_2O_2 system may be attributed to the trapping of the photo-generated conduction band electrons of TiO_2 by H_2O_2, which is more efficient than trapping by O_2. It is also well known that H_2O_2 photo-decomposes easily generating

hydroxyl radicals (·OH) which participate in the overall oxidative process. In our system (visible light/TiO$_2$–Fe^{3+}/H$_2$O$_2$), the presence of H$_2$O$_2$ led to a higher rate of degradation due to the synergism of electron scavenging action of H$_2$O$_2$ (Eq. 3) and hydroxyl production by photolysis of H$_2$O$_2$ (Eq. 4) [37].

$$H_2O_2 + e^- \rightarrow HO \cdot + HO^-, \quad (3)$$

$$H_2O_2 \xrightarrow{h\nu} 2HO. \quad (4)$$
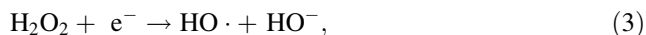
On the other hand, iron ion can act as both hole and electron traps according to the following reactions (Eqs. 5–8): [38]

$$Fe^{3+} + e^- \rightarrow Fe^{2+}, \quad (5)$$

$$Fe^{2+} + O_{2(ads)} \rightarrow Fe^{3+} + O_2^-, \quad (6)$$

$$Fe^{2+} + Ti^{4+} \rightarrow Fe^{3+} + Ti^{3+}, \quad (7)$$

$$Fe^{3+} + h_{vb}^+ \rightarrow Fe^{4+}. \quad (8)$$

These reactions could enhance the photocatalytic performance of the photocatalyst when the amount of iron doping is appropriate. Excessive doping can be detrimental for the photoactivity of the catalyst, since iron(III) ions could act as additional recombination centers and quenching electron transfer [39]. In our system, we observe

iron dissolution during the mineralization of MO and MB. The photo-dissolution of the ions reduces the additional recombination centers and give rise to a homogeneous (Fenton like)-heterogeneous photocatalytic system with improved photoactivity.

Toxicity studies

Despite the numerous laboratory studies and technical applications of nano-structured titanium dioxide based materials (NSTDM), studies regarding evaluation of their toxicity are very scarce [40, 41]. Because their numerous applications, NSTDM enter the environment and get in contact with biota and human beings, making imperative to elucidate their possible health effects. For instance, data from a wastewater treatment plant showed raw sewage to contain 10–100 µg/L Ti. Besides, due to low solubility, titanium containing compounds adsorb to biomass resulting in the production of bio-solids that present large quantities of NSTDM [42].

Since NSTDM exert activity upon radiation, light is an important variable to consider during the evaluation of the toxicity of these materials. Because hemolysis of erythrocytes is a rapid and sensitive method to examine the effects of micro-structured solids on cell membrane and allows to

Fig. 11 Evaluation of hemolytic activity of TiO$_2$–Fe^{3+} 1 % nano-structured materials under different conditions. a RBC dilution under illumination and 24 °C. b RBC dilution in the dark and 24 °C. c Whole blood under illumination and 24 °C. d Whole blood in the dark and 24 °C

conduct the study under several experimental conditions (in the dark, under radiation, at variable temperature, etc.), we decided to initiate a systematic study of the effects caused by TiO_2–Fe^{3+} on mammalians, using human red blood cells (HRBC) as starting point of the study. Our results are schematically presented in Fig. 11. It is readily seen that TiO_2–Fe^{3+} nano-structured powders do not exert toxic effects on HRBC. Despite the small size of the materials, hemolysis of erythrocytes did not occur even in radiated solutions after 12 h of exposition. Iron ion is not present in saline solution after evaluation of hemolytic activity of the materials.

Different concentrations of TiO_2–Fe^{3+} materials were evaluated; our results indicate that the bare TiO_2 and iron-doped TiO_2 under study do not show toxicity to HRBC at concentrations up to 1 mg/mL when whole blood is used for the study. On the other hand, when the study is carried using isolated erythrocytes suspended in PSS, hemolysis of cells is observed. The hemolytic activity increases when the solutions are radiated. The percent of hemolysis observed increases linearly with the amount of nano-structured material evaluated. Results are summarized in Fig. 12. For concentrations up to 1 mg/mL, the following data were obtained: In the dark, 6.32, 4.5, and 5.9 % of hemolysis for TiO_2–Fe^{3+} 1, 3, and 5 %, respectively. Under illumination, 7.51, 7.3, and 9.3 % of hemolysis for TiO_2–Fe^{3+} 1, 3, and 5 % was observed. It was clearly observed that bigger amounts of materials result in higher percent of hemolysis to erythrocytes, but the effect of increasing doping level cannot be easily inferred at this point. From UV–Vis analysis, it is found that light
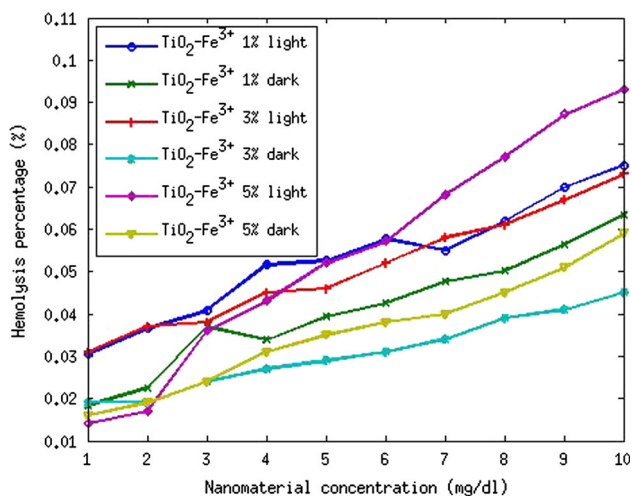
absorptivity of TiO_2–Fe^{3+} decreases as 1 > 3 > 5 % that in part explains the higher hemolytic activity of 1 % doped materials; since these materials present more capacity to absorb light a higher photocatalytic activity should be expected. Since HRBCs are present in PSS as "naked" cells, they are susceptible to oxidative degradation. When whole blood is evaluated, plasma protects HRBCs from degradation activity of materials.

Emerging literature suggests that dissolution of nanomaterials in biological fluids favors its cellular uptake and can be directly linked to the toxic effects of the materials [13, 43]. Because photo-dissolution of iron ions was observed during photocatalytic treatment, the leaching of iron into the physiological solution was evaluated. Iron ion was not present in solution; by comparing, during photocatalytic activity, evaluation iron ion was released and found in the remaining solution. It is thus expected that photo-bleaching of iron ions should occur in HRBC/saline solution mixtures. The absence of iron ion in the remaining solution suggests that under these conditions, as the iron ion is released, HRBC uptake it. Because iron is a component of hemoglobin, this element can be stored in ferritin without causing deleterious effects on cells. Blood compatibility studies of nano-structured iron oxides materials report on negligible hemolysis activity of the materials [44, 45] which is in agreement with the observed results of this study.

To date, it is difficult to establish a strong relationship regarding the composition and toxicity of nanomaterials, since its bioactivity depends on the size, structure, physicochemical, and surface properties. For instance, the in vivo and in vitro toxicity of rutile TiO_2–Fe^{3+} nanorods was recently evaluated [46]. In vivo toxicity evaluation, using Wistar rats as model organism, showed that pulmonary exposure to rutile TiO_2–Fe^{3+} nanorods promotes pulmonary and systemic inflammation, oxidative stress, and hepatotoxicity. Besides, this material showed direct toxicity on human lung cancer cells and human hepatoma cells.

Nowadays, there are no specific testing guidelines for evaluation of nanotoxicity, so the U.S. EPA or OECD guidelines for chemical testing are frequently followed. Due to the lack of standard protocols, experimental conditions are highly variable among research groups, and results cannot be meaningfully compared when parameters like dose, exposure time, endpoint assay, and evaluation model differ [12]. However, according to the "cradle to grave" approach, all of the impacts of a new technology, from manufacturing to disposal, are relevant to its sustainability [47]. Since we are looking for the macro scale application of TiO_2–Fe^{3+} supported materials, this study indicates that the material under study shows no toxicity to HRBC. The in vivo toxicity of the materials is currently being evaluated.

Fig. 12 Determination of the percentage of hemolytic activity of iron-doped TiO_2 materials. Degree of hemolysis caused by TiO_2–Fe^{+3} nano-structured materials to erythrocytes. The percent of hemolysis increased as a function of increasing mass concentration of particles in the PSS/HRBC mixture

Conclusion

Iron-doped titanium dioxide materials were synthesized and fully characterized. Electron microscopy analysis demonstrated the nanometric nature of these materials. Photo-bleaching of iron ions can be indicative of segregation of iron oxides to the surface of the catalyst. The amount of iron ions in solution increases as the doping level increases, indicating that due to the large amount of iron load in the materials, only a small portion of iron ion incorporates within the TiO_2 lattice segregating the excess to the surface of the materials. Surface iron ions are prone to photo-dissolution giving rise to a homogeneous (Fenton like)-heterogeneous (Fe^{+3}–TiO_2) mediated mechanism for the degradation of pollutants. The prepared materials do not exhibit hemolytic activity against HRBCs. The obtained results demonstrate potential of iron-doped TiO_2 materials to be used in solar-driven water purification systems.

References

1. Chatterjee D, Dasgupta S (2005) Visible light induced photocatalytic degradation of organic pollutants. J Photochem Rev 1–2:186–205

2. Hoffmann MR, Martin ST, Choi W, Bahnemann DW (1995) Environmental applications of semiconductor photocatalysis. Chem Rev 95(1):69–96

3. Chen X, Mao SS (2007) Titanium dioxide nanomaterials: synthesis, properties, modifications and applications. Chem Rev 107(7):2891–2959

4. Yamashita H, Harada M, Misaka J, Takeuchi M, Ikeue K, Anpo M (2002) Degradation of propanol diluted in water under visible light irradiation using metal ion-implanted titanium dioxide photocatalysts. J Photochem Photobiol A 148:257–261

5. Dukes FM, Iuppa E, Meyer B, Mary Jane Shultz MJ (2012) Differing photo-oxidation mechanisms: electron transfer in TiO_2 versus iron-doped TiO_2. Langmuir 28:16933–16940

6. Adán C, Bahamonde A, Fernández-García M, Martínez-Arias A (2007) Structure and activity of nanosized iron-doped anatase TiO_2 catalysts for phenol photocatalytic degradation. Appl Catal B Environ 72:11–17

7. Litter MI, Navio JA (1996) Photocatalytic properties of iron-doped titania semiconductors. J Photochem Photobiol A Chem 98:171–181

8. Liu M, Qiu X, Miyauchi M, Hashimoto K (2013) Energy-level matching of Fe(III) ions grafted at surface and doped in bulk for efficient visible-light photocatalyst. J Am Chem Soc 135:10064–10072

9. Rawal B, Kim HJ, Lee WI (2013) Enhanced visible-light photocatalytic properties of Fe^{+3}-grafted N-doped TiO_2 nanoporous spheres. Appl Catal B Environ 142–143:458–464

10. Esquivel K, Nava R, Zamudio-Mendez A, Vega González M, Jaime-Acuña OE, Escobar-Alarcón L, Peralta-Hernández JM, Pawelec B, Fierro JLG (2013) Microwave-assisted synthesis of (S)Fe/TiO_2 systems: effects of synthesis conditions and dopant concentration on photoactivity. Appl Catal B Environ 140–141:213–224

11. Zhao B, Mele G, Pio I, Palmisano L, Vasapollo G (2010) Degradation of 4-nitrophenol (4-NP) using Fe–TiO_2 as a heterogeneous photo-Fenton catalyst. J Hazard Mater 1–3:569–574

12. Schrand AM, Dai L, Schlager JL, Hussain SM (2012) Toxicity testing of nanomaterials. In: Balls M, Combes RD, Bhogal N (eds) New technologies for toxicity testing. Springer, New York, pp 58–75

13. Pokhrel S, Nel AE, Madler L (2013) Custom-designed nanomaterial libraries for testing metal oxide toxicity. Acc Chem Res 46(3):632–641

14. Saquib Q, Al-Khedhairy A, Siddiqui MA, Abou-Tarboush F, Azam A, Musarrat J (2012) Titanium dioxide nanoparticles induced cytotoxicity, oxidative stress and DNA damage in human amnion epithelial (WISH) cells. Toxicol In Vitro 26(2):351–361

15. Medina-Ramírez I, Luo Z, Bashir S, Mernaugh R, Liu JL (2011) Facile design and nanostructural evaluation of silver-modified titania used as disinfectant. Dalton Trans 40:1047–1054

16. Mackenzie JD, Bescher EP (2007) Chemical routes in the synthesis of nanomaterials using the sol–gel process. Acc Chem Res 40(9):810–818

17. Bloh J, Dillert R, Bahnemann D (2012) Designing optimal metal-doped photocatalysts: correlation between photocatalytic activity, doping ratio, and particle size. J Phys Chem C 116:25558–25562

18. Zhang Z, Wang C, Zakaria R, Ying J (1998) Role of particle size in nanocrystalline TiO_2-based photocatalysts. J Phys Chem B 102(52):10871–10878

19. Zhang J, Hu Y, Matsuoka M, Yamashita H, Minagawa M, Hidaka H, Anpo M (2001) Relationship between the local structures of titanium oxide photocatalysts and their reactivities in the decomposition of NO. J Phys Chem B 105(35):8395–8398

20. Aydin C, El-sadek MS, Zheng K, Yahia IS, Yakuphanoglu F (2013) Synthesis, diffused reflectance and electrical properties of nanocrystalline Fe-doped ZnO via sol–gel calcination technique. Opt Laser Technol 48:447–452

21. Zhang W, Chen Y, Yu S, Chen S, Yin Y (2008) Preparation and antibacterial behavior of Fe^{3+}-doped nanostructured TiO_2 thin films. Thin Solid Films 516(15):4690–4694

22. Wang B, Li Q, Wang W, Li Y, Zhai J (2011) Preparation and characterization of Fe^{3+}-doped TiO_2 on fly ash cenospheres for photocatalytic application. Appl Surf Sci 257(8):3473–3479

23. Wang JA, Limas-Ballesteros R, López T, Moreno A, Gómez R, Novaro O, Bokhimi X (2001) Quantitative determination of titanium lattice defects and solid-state reaction mechanism in iron-doped TiO_2 photocatalysts. J Phys Chem B 105:9692–9698

24. Wang XH, Li J-G, Kamiyama H, Moriyoshi Y, Ishigaki T (2006) Wavelength-sensitive photocatalytic degradation of methyl orange in aqueous suspension over Iron(III)-doped TiO_2 nanopowders under UV and visible light irradiation. J Phys Chem B 110:6804–6809

25. Di Paola A, Marci G, Palmisano L, Schiavello M, Uosaki K, Ikeda S, Othani B (2002) Preparation of polycrystalline TiO_2 photocatalysts impregnated with various transition metal ions: characterization and photocatalytic activity for the degradation of 4-nitrophenol. J Phys Chem B 106:637–645

26. Shao-You L, Qun-Li T, Qing-Ge F (2011) Synthesis of S/Cr doped mesoporous TiO_2 with high-active visible light degradation property via solid state reaction route. Appl Surf Sci 257(13):5544–5551

27. Mangham AN, Govind N, Bowden ME, Shutthanandan V, Joly AG, Henderson MA, Chambers SA (2011) Photochemical

properties, composition and structure in molecular beam epitaxy grown Fe "doped" and (Fe, N) codoped rutile TiO_2 (110). J Phys Chem C 115(31):15416–15424

28. Li H, Liu G, Chen S, Liu Q (2010) Novel Fe doped mesoporous TiO_2 microspheres: ultrasonic–hydrothermal synthesis, characterization, and photocatalytic properties. Phys E 42(6):1844–1849

29. Poulin S, Franca R, Moreau-Bélanger L, Sacher E (2010) Confirmation of X-ray photoelectron spectroscopy peak attributions of nanoparticulate iron oxides, using symmetric peak component line shapes. J Phys Chem C 114(24):10711–10718

30. Houas A, Lachheb H, Guillard Ch, Herrmann J-M (2001) Photocatalytic degradation pathway of methylene blue in water. Appl Catal B Environ 31:145–157

31. Guivarch E, Trevin S, Lahitte C, Oturan MA (2003) Degradation of azo dyes inwater by electro-Fenton process. Environ Chem Lett 1:38–44

32. Dai K, Chen H, Peng T, Ke D, Yi H (2007) Photocatalytic degradation of methyl orange in aqueous suspension of mesoporous titania nanoparticles. Chemosphere 69(9):1361–1367

33. Raileanu M, Crisan M, Nitoi I, Ianculescu A, Oancea P, Crisan D, Todan L (2013) TiO_2-based nanomaterials with photocatalytic properties for the advanced degradation of xenobiotic compounds from water. A literature survey. Water Air Soil Pollut 224:1548

34. Teh C, Mohamed A (2011) Roles of titanium dioxide and ion-doped titanium dioxide on photocatalytic degradation of organic pollutants (phenolic compounds and dyes) in aqueous solutions: a review. J Alloys Compd 509(5):1648–1660

35. Cong Y, Zhang J, Chen F, Anpo M, He D (2007) Preparation, photocatalytic activity, and mechanism of nano-TiO_2 Co-doped with nitrogen and iron (III). J Phys Chem C 111:10618–10623

36. Sadik WA (2007) Effect of inorganic oxidants in photodecolourization of an azo dye. J Photochem Photobiol A Chem 191(2–3):132–137

37. Legrini O, Oliveros E, Braun AM (1993) Photochemical processes for water treatment. Chem Rev 93:671–698

38. Elghniji K, Atyaoui A, Livraghi S, Bousselmi L, Giamello E, Ksibi M (2012) Synthesis and characterization of Fe^{3+} doped TiO_2 nanoparticles and films and their performance for photocurrent response under UV illumination. J Alloys Compd 541:421–427

39. Veréb G, Ambrus Z, Pap Zs, Kmetykó A, Dombi A, Danciu V, Cheesman A, Mogyrósi K (2012) Comparative study on UV and visible light sensitive bare and doped titanium dioxide photocatalysts for the decomposition of environmental pollutants in water. Appl Catal A Gen 417–418:26–36

40. Zhang R, Bai Y, Zhang B, Chen L, Yan B (2012) The potential health risk of titania nanoparticles. J Hazard Mater 211–212:404–413

41. Gajewicz A, Rasulev B, Dinadayalane T, Urbaszek P, Puzyn T, Leszczynska D, Leszczynski J (2012) Advancing risk assessment of engineered nanomaterials: application of computational approaches. Adv Drug Deliv Rev 64(15):1663–1693

42. Kiser M, Westerhoff P, Benn T, Wang Y, Perez-Rivera J, Hristovski K (2009) Titanium nanomaterial removal and release from wastewater treatment plants. Environ Sci Technol 43(17):6757–6763

43. Auffan M, Rose J, Wiesner M, Bottero J (2009) Chemical stability of metallic nanoparticles: a parameter controlling their potential cellular toxicity in vitro. Environ Pollut 157:1127–1133

44. Wu H, Zhang S, Zhang J, Liu G, Shi J, Zhang L, Cui X, Ruan M, He Q, Bu W (2011) A hollow-core, magnetic, and mesoporous double-shell nanostructure. In situ decomposition/reduction synthesis, bioimaging, and drug-delivery properties. Adv Funct Mater 21(10):1850–1862

45. Behera T, Swain P, Rangacharulu P, Samanta M (2013) Nano-Fe as feed additive improves the hematological and immunological parameters of fish, *Labeo rohita* H. Appl Nanosci. doi:10.1007/s13204-013-0251-8

46. Nemmar A, Melghit K, Al-salam S, Zia S, Dhanasekaran S, Attoub S, Al-Amri I, Ali B (2011) Acute respiratory and systemic toxicity of pulmonary exposure to rutile Fe-doped TiO_2 nanorods. Toxicology 279(1–3):167–175

47. Miralles P, Church T, Harris A (2012) Toxicity, uptake, and translocation of engineered nanomaterials in vascular plants. Environ Sci Technol 46(17):9224–9239